EFFECT OF SYNTHETIC JET PARAMETERS ON CONTROLLED FLOW OVER AN AIRFOIL

T. Parthasarathy[1] & S.P. Das[2,*]

[1]*University of Illinois at Urbana-Champaign, Urbana, Illinois 61820, USA*

[2]*Indian Institute of Technology Madras, Chennai 600036, India*

*Address all correspondence to: S.P. Das, Indian Institute of Technology Madras, Chennai 600036, India,
 E-mail: spdas@iitm.ac.in

Flow control for performance enhancement over airfoils (both stall and load enhancement) has become an increasingly important topic. This numerical work describes the characteristics of flow control using synthetic jets over a NACA 0015 airfoil at a Reynolds number of 8.96×10^5 (based on the chord length and free-stream velocity) and at 20° angle of attack (wherein the flow is separated). A range of synthetic jet parameters were chosen to visualize their effects on the controlled flow. Analysis of key flow parameters indicate that the synthetic jet is efficient in increasing the lift coefficient while simultaneously reducing the drag coefficient, more so for larger jet amplitudes and at smaller angles of jet injection. A regression model for predicting the flow parameters is also specified. Toward the end of the study, a new parameter—the differential time of suction and blowing—was identified and its effect on the flow dynamics was observed. While the time modulation offers some benefits, it is the opinion of the authors that the benefits are too marginal to justify the implementation of such a system. This work serves as a platform to qualitatively and quantitatively understand the effects of the jet parameters on the separated flow over the airfoil, by understanding the flow parameters and structures.

KEY WORDS: *flow control, synthetic jet, vortex dynamics, unsteady aerodynamics, jet–cross-flow interaction*

1. INTRODUCTION

The performance of an airplane wing, and thus an airfoil, binds the aeronautical industry—be it in energy expenditure, noise, or emission levels. This performance is usually coupled with two important aspects: the load control over a wide range of angles of attacks and the delay of flow separation on its surface (thus leading to higher stall angles). This performance depends on a multitude of factors. To an extent, the design of the airfoil is crucial in determining its performance. However, the use of exotic airfoil profiles is limited, due to orthogonal constraints in material selection, manufacturability, and cost. In spite of this limitation, we have found ways to reap benefits, such as high lift and less thrust. The aforesaid performance enhancement can be effectively achieved by using flow control techniques, as highlighted in the past (Jahanmiri, 2010). Flow control is defined as the ability to alter the character or disposition of a natural flow field actively or passively in order to effect a desired change.

Passive flow control devices, such as flaps and vortex generators, have been effective in reducing flow separation under limited conditions (Jirasek, 2005). Although these devices require no additional energy expenditure, they are unable to adapt to changes occurring in the flow system. This causes degradation in performance in cruise conditions (when no flow separation occurs). Active flow control techniques, however, are very adaptive to external flow conditions and are hence extremely popular, despite the penalty on extra energy expenditure. Active flow control encompasses a variety of techniques, ranging from continuous blowing, continuous suction, and periodic oscillations, among others. Continuous blowing and suction (De Giorgi et al., 2015) incorporates traditional ideas on preventing flow separation. Flow separation usually takes place in case a low-momentum flow is present near the solid

surface. Both continuous suction and continuous blowing aim to do the same, but by different means. While this is an attractive option in theory (as it produces effective control) it fails in implementation due to its bulky nature and the comprehensive piping systems and fluid inlet/outlet required.

Unsteady active flow control has been an actively pursued area of research in the past decades. A major advantage of such an unsteady control technique is that it can exploit the existing instabilities in the flow (Collis et al., 2004). Periodic excitation accelerates and regulates the generation of large coherent structures with the flow and hence transfers high-momentum fluid across the mixing layer. Of particular interest in periodic excitation control is the use of zero net mass flux devices, also called synthetic jets (Glezer and Amitay, 2002). Synthetic jets are formed by oscillatory flow through an orifice. Hence they offer no mass addition (or removal), entrain low-momentum fluid, and promote mixing through the formation of vortical structures. This means that they are compact, use less energy (as they exploit the instabilities in the flow), and are effective. The performance of the synthetic jets in controlling a flow greatly relies on its key parameters—the amplitude, frequency, jet inclination angle, location of the synthetic jets, to name a few (Mittal and Rampunggoon, 2002; Okada et al., 2009; Akcayoz and Tuncer, 2009).

Numerical simulations are best suited to undertake an elaborate parametric study based on the synthetic jet parameters. This can be attributed to the disadvantages of doing the same experimentally: cost, complexity, and lack of conclusive clarity. While such complex unsteady flows are best predicted by methods such as large eddy simulations (LES), Reynolds-averaged Navier–Stokes Equation (RANS) based solutions offer adequate accuracy which can be used to investigate associated physics (Iaccarino et al., 2004).

Several experimental and numerical works in characterizing the flow control over an airfoil have been done in the past. Experimental data for the same airfoil at different angles of attack for a Reynolds number (Re $= U_\infty C/\nu$, where U_∞ is the free-stream velocity, C is the chord length, and ν is the kinematic viscosity) of 896,000 (Gilarranz et al., 2005) suggest that the maximum lift coefficient value can be enhanced by 80% and the stall angle can be pushed back from 12° to 18°. Other such experiments also conclusively prove that synthetic jets are indeed effective in affecting the flow environment (Goodfellow et al., 2012; McCormick, 2000). Numerical studies also demonstrate and characterize the effect of synthetic jets on a wide range of airfoils at different angles of attack (Raju et al., 2008; You and Moin, 2008; Lasagna et al., 2013). Another similar numerical study (Duvigneau and Vissoneau, 2006) explores the effect of some jet parameters on the lift and drag coefficients for a NACA 0015 airfoil at the same Reynolds number, and suggests an increase in the lift by as much as 34%.

In the present study, numerical investigations have been carried out to understand the effects of the synthetic jet parameters on the external flow over a NACA 0015 airfoil. Thrust is given in understanding the reason behind the performance enhancement on using the synthetic jets in such separated flows. A commercial RANS code (FLUENT) utilizing an unstructured grid was employed to simulate the flow over an airfoil that has a jet actuator implanted in it. In Section 2, the computational method and the flow configuration are listed and a benchmark comparison between the present work and a previous work (Duvigneau and Vissoneau, 2006) is made. The effect of the jet parameters on the external flow and the resulting physics is elaborated in Section 3. Concluding observations and future directions are mentioned in Section 4.

2. METHOD

2.1 Numerical Method

The numerical algorithm and solution methods of the commercial code FLUENT, provided by ANSYS Inc., are used to investigate the phenomenon. The incompressible Navier–Stokes equations after averaging are

$$\frac{\partial \bar{u}_i}{\partial t} + \frac{\partial}{\partial x_j}\left(\bar{u}_i \bar{u}_j\right) + \frac{\partial \tau_{ij}}{\partial x_j} = -\frac{\partial \bar{p}}{\partial x_i} + \frac{1}{\text{Re}}\frac{\partial}{\partial x_j}\frac{\partial \bar{u}_i}{\partial x_j} \tag{1}$$

$$\frac{\partial \bar{u}_i}{\partial x_i} = 0 \tag{2}$$

where τ_{ij} is the Reynolds stress tensor modeled by the Spalart–Allmaras model in this case (Spalart and Allmaras, 1992). While the Spalart–Allmaras one-equation model does not perform well in predicting isotropic turbulent decay,

it performs fairly well in documenting effects associated with such flows. It has also been advocated that employing two-equation models offer no significant benefits. A comparative study of different models for the particular case of unsteady high-speed aerodynamic flow over airfoils was also run and no significant difference was observed. The Spalart–Allmaras model was thus an attractive option as for similar accuracy, only one turbulent quantity rather than two needs to be solved for, accelerating the performance of the code. The coordinates, velocity, pressure, and time are normalized by the airfoil chord length C, the free-stream velocity U_∞, and the dynamic pressure term ρU_∞^2 and C/U_∞, respectively. Discretization of spatial elements is done using an upwind scheme that results in a second-order accuracy using linear reconstruction. A second-order fully implicit integration scheme in time is used to resolve the temporal scales. The solver utilizes a pressure correction equation to satisfy the continuity equation (2), coupled with the velocity variables using the well-tested SIMPLE algorithm. At a particular time step, the solver is run either until the normalized residuals decreases to at least three orders of magnitude or until a particular number of iterations is attained—whichever is satisfied last. The solver then proceeds with the iteration corresponding to the next time step and the entire process is repeated again. The solver is stopped when a quasi-steady state solution (a solution that repeats itself periodically) is reached.

2.2 Flow Configuration

2.2.1 Geometric Details

Figure 1 details the flow configuration and the dimensions of the airfoil and the jet. This is a similar setup tested earlier (Gilarranz et al., 2005; You and Moin, 2008) but does not include blocking. A NACA 0015 airfoil with chord length (C) of 0.375 m is used. The synthetic jet is fixed at 12% of the chord measured from the leading edge (Lasagna et al., 2013) and it opens into the suction side of the airfoil. Based on previous studies (Dannenberg and Weiberg, 1952), the width (w) of the jet opening is suitably chosen to be 0.53% of the chord length. Sufficient spacing is given so that the outflow boundary conditions do not significantly alter the flow over the airfoil, as seen in Fig. 1, which also specifies
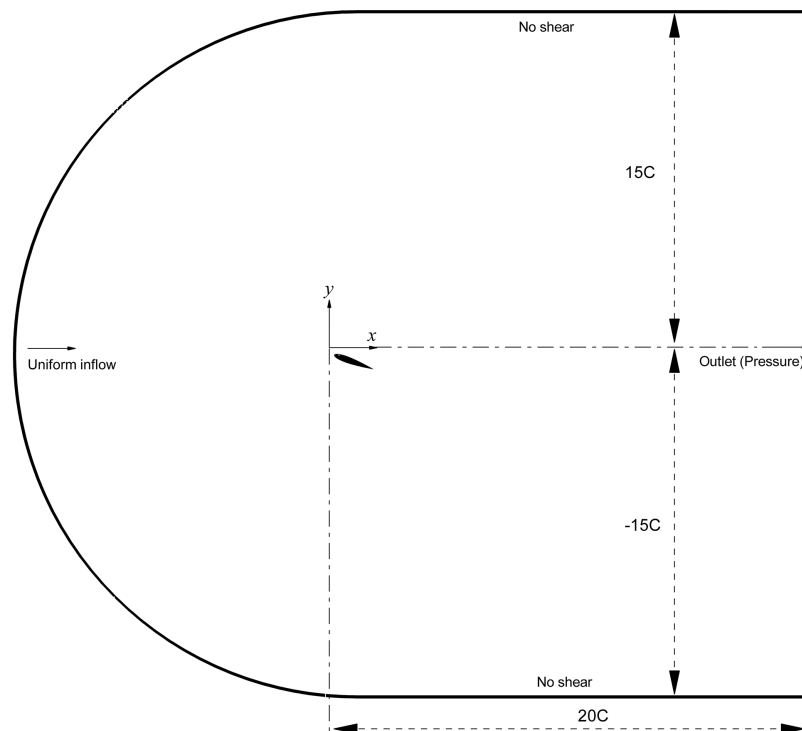

FIG. 1: Flow configuration and geometry for the flow over a NACA 0015 airfoil with synthetic jet

the necessary boundary conditions. The computational domain is hence of size $35C \times 30C$. A no-slip boundary condition is applied on the airfoil surface and the cavity walls and a pressure outflow condition for the velocity is applied at the exit. The pressure outlet boundary condition is generally applied when a "free" boundary is required in an external flow. A no-shear condition is applied on the top and the bottom walls to simulate open conditions. It is prudent to specify that the synthetic jet is modeled along with the cavity, as previous studies (Raju et al., 2009) have shown that this gives the best results. The jet is modeled with two walls on the side, and a time-varying sinusoidal boundary condition is given at the sinusoidal velocity inlet shown in Fig. 2, in such a way that at the jet exit, the flow is fully developed and has the desired exit jet velocity. This is detailed later.
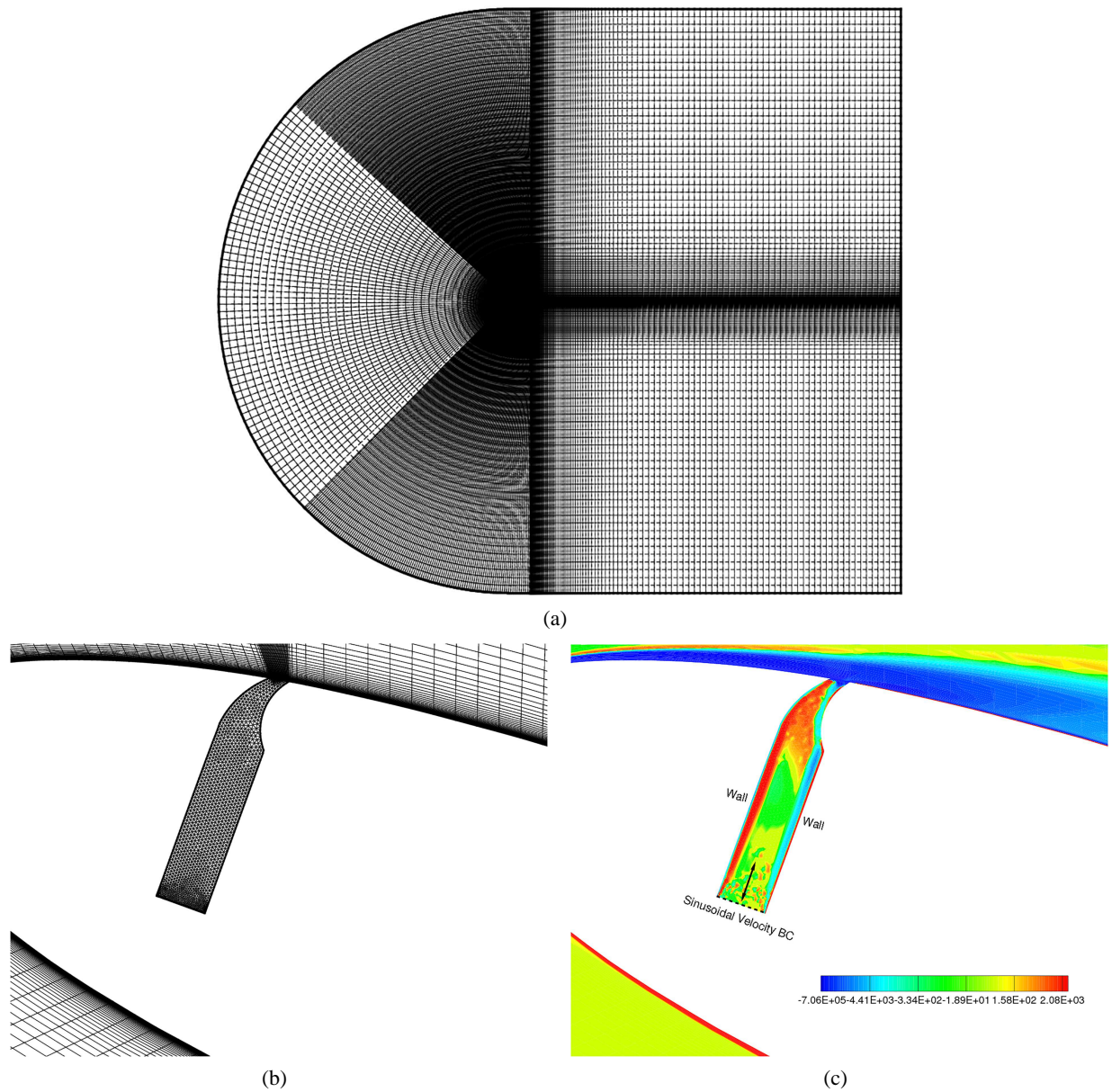

(a)

(b)

(c)

FIG. 2: (a) Representative mesh; (b) close-up of the mesh with the embedded synthetic jet actuator; (c) boundary conditions and vorticity contours for a representative case

2.2.2 Grid Details

A two-dimensional unstructured grid is employed, and is deemed sufficient enough, based on previous studies (Kitsios et al., 2006). The computational grid employed changes for different angles of jet, as the geometry changes. However, the number of nodes is kept nearly the same over the different meshes. A C-Grid is used to capture the physics associated with the flow, and is refined as the mesh approaches the airfoil wall. The number of grid points placed on the semi-circular inlet, horizontal, and vertical edges, are 363, 120, and 240, respectively. As represented in Fig. 1, the semi-circular inlet has a radius of $15C$ with 363 points distributed equally across, giving a circumferential spacing of $0.13C$. The horizontal spacing on the top (and bottom) edge varies and is $0.001C$ closest to the airfoil wall and grows with a constant ratio of 1.1 as it goes away from the wall. Similarly the vertical spacing differs, from near $0.001C$ beside the wall and grows with a constant ratio of 1.1. The mesh is shown in Fig. 1. Three different meshes were chosen to study the effect of the grid on the flow: Mesh I, with 35,200 cells; Mesh II, with 74,879 cells, and Mesh III, with 144,000 cells. A grid independence study is done with all the aforementioned grids (I, II, and III) (Fig. 3), base on which Mesh II is employed for further calculations. The mesh is constructed to capture the physics associated with the flow near the cavity, and hence the mesh is concentrated there, with as much as 20 mesh points allocated along the cavity slot. The spacing value $(\Delta c/C)$ near the jet exit is 2.01×10^{-4}, at the point of maximum (near the airfoil wall) is 7.36×10^{-3}, and normal to the wall is 2.6×10^{-5} corresponding to a y^+ value of 1). The mesh is radial in the semi-circular region and is concentrated as mentioned above at the jet opening. At the wake of the airfoil and normal to the wake, the mesh consists of rectangular elements. The simulation uses a maximum time step of $(\Delta t U_\infty/C)$ of 7.7×10^{-3}, corresponding to Courant–Friedrichs–Lewy (CFL) numbers close to 1 in most of the computational domain.

2.2.3 Flow Details

An inlet velocity of 34.9 m/s, with very low turbulent intensity (∼1%), is specified to achieve a flow of Reynolds number 8.96×10^5 ased on the chord length, for which data are available for comparison. Based on the previously selected grid, a comparison of the lift coefficient against the angle of attack is made with a previous work (Duvigneau and Vissoneau, 2006), as shown in Fig. 4. Comparison is made with a numerical work rather than an experimental work (Gilarranz et al., 2005) because of several reasons. These are highlighted in previous works (Ravindran, 1999; Donovan et al., 1998), but is reproduced here for the sake of clarity. First, we compute a fully turbulent flow, while the Reynolds number corresponds to a regime where transition effects might play an important role. Second, the
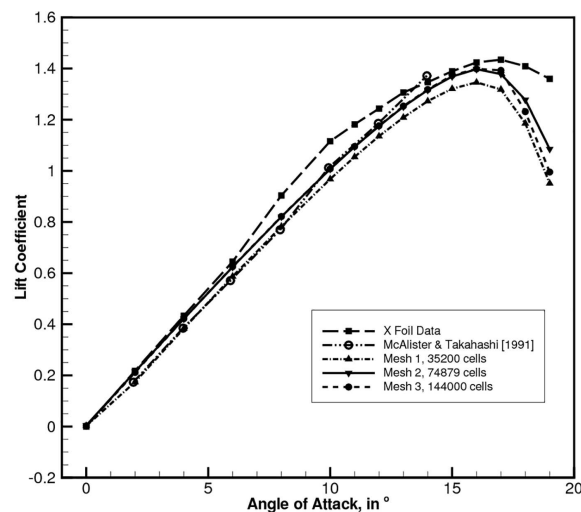

FIG. 3: Grid independence study on the uncontrolled flow over the NACA 0015 aerofoil. Also shown is the comparison of numerical data adapted from Drela (1989) and experimental data adapted from McAlister and Takahashi (1991)
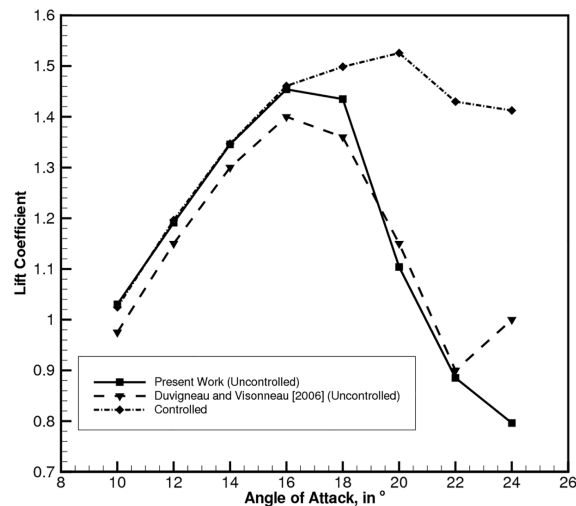
FIG. 4: Comparison of the results of the present study adapted from Collis et al. (2004)

experiments (Gilarranz et al., 2005) conducted in a wind tunnel have significant blocking effects courtesy of the height of the wind tunnel, which is only 2.3 times the chord length. The same argument can be made for the effect of finite width of the wind tunnel on the measured data. The purpose of the present study is to understand the effect of the jet parameters in a free-stream flow, and as such, comparison to experiment does not seem to be critical. A good match is obtained, indicating that the present solver is indeed capable of simulating the flow reasonably well. The present study will focus on the case with 20° angle of attack, where leading edge type separation occurs and the location of separation is just near the location of the synthetic jet (Lasagna et al., 2013).

2.2.4 Synthetic Jet Details

As mentioned before, the synthetic jet is modeled as a velocity inlet with a sinusoidal boundary condition. Of importance is the value of the jet exit velocity (V_j), the jet frequency (f), the angle of injection normal to the wall (θ), and the new parameter to be explored—the differential suction and blowing times within a cycle time (t_{suc} and t_{blow}). The non-dimensional parameters that will correspondingly be used in the rest of the present study: amplitude ratio at jet exit ($VR = V_j/U_\infty$), non-dimensional frequency ($F = fC/U_\infty$), and the suction parameter ($k = t_{suc}/t_{blow}$). The jet location and width are fixed based on previous studies (Lasagna et al., 2013; Duvigneau and Vissoneau, 2006). The model of the synthetic jet is constructed, akin to the original piston cylinder setup used in the experiments (Gilarranz et al., 2005), such that the jet exit velocity can be represented in terms of the dimensional parameters as given below. The jet contributes to net zero mass flux (the integral over one cycle of jet operation is zero), while adding momentum flux (and consequently vorticity flux) to the external flow.

$$(u, v, w)_{jet-inlet} = (\cos(\alpha), \sin(\alpha), 0) \, V_j \, (\sin(2\pi f t)) \tag{3}$$

Apart from the aforesaid non-dimensional parameters, an additional (one among many such) parameter called the jet momentum coefficient is quite useful in characterizing the jet, and is defined as

$$C_\mu = \frac{hV_j^2 \sin(\theta)}{CU_\infty^2} \tag{4}$$

The range of parameters tested in this particular study is listed in Table 1 and the corresponding jet momentum coefficients are given in Table 2.

The amplitude ratios of magnitude greater than 2.25 are not possible due to the high velocities involved (Akcayoz and Tuncer, 2009). Furthermore, the range of non-dimensional frequencies tested is limited to $\sim O(1)$ and literature indicates varied physics at higher non-dimensional frequencies (Raju et al., 2008).

TABLE 1: Summary of parameters

Non-dimensional frequency $(F = fC/U_\alpha)$	Amplitude ratio at jet exit $(VR = V_j/U_\alpha)$	Angle of jet injection $(\theta, \text{in }°)$	Suction parameter (k)
0.6446	1.5	30	0.25
0.967	2	45	0.5
1.1281	2.25	60	1
1.2893	2.5	90	2
1.6117	3	—	4

TABLE 2: Jet momentum coefficient

C_μ		Angle $(\theta, \text{in }°)$			
		30	**45**	**60**	**90**
	1.5	0.006	0.0085	0.0104	0.012
	2	0.0107	0.0151	0.0185	0.0213
Amplitude Ratio (VR)	2.25	0.0135	0.0191	0.0234	0.027
	2.5	0.0167	0.0236	0.0289	0.0333
	3	0.024	0.0339	0.0416	0.048

3. RESULTS

The results of the parametric study—the quantitative and qualitative aspects, and the flow physics acquired—are detailed here in the aforementioned order, for all the parameters varied. For the sake of brevity, only the important facets are presented and conclusions are drawn from the same. The lift and the drag values for the airfoil are obtained after a quick control volume analysis.

3.1 Lift and Drag Characteristics

As specified earlier, the characteristics are observed once the system reaches a quasi-steady state. This means that the quantitative characteristics are also periodic and hence need to be averaged over a time period to obtain the mean values. One such example is given in Fig. 5. Figure 6 gives necessary details of the effect of the amplitude ratio,
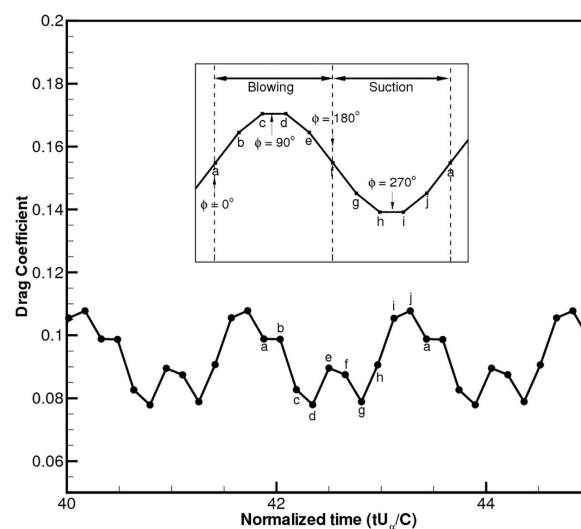

FIG. 5: History of the characteristic coefficients on the aerofoil wall
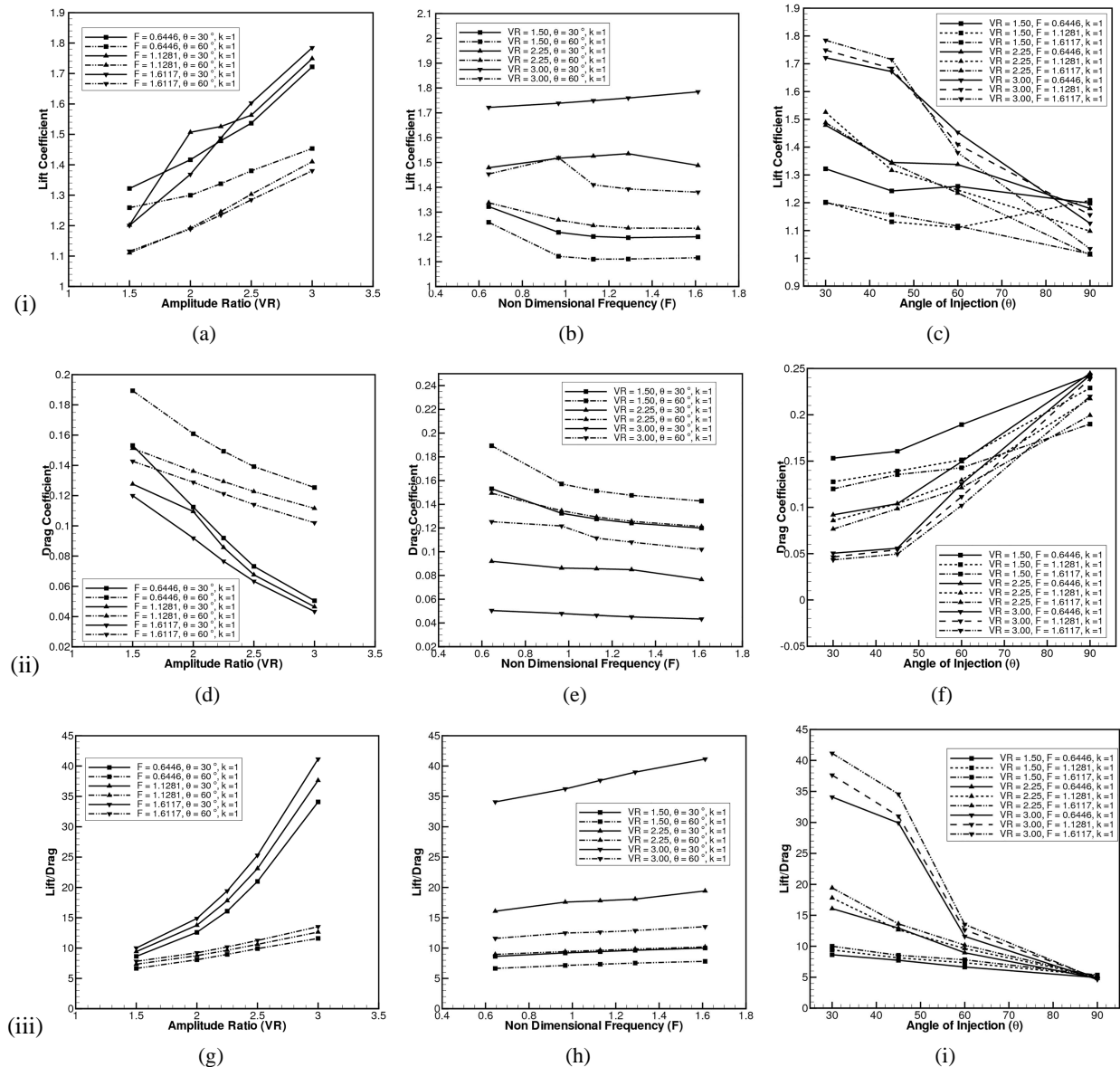
FIG. 6: Parametric study of the unmodulated ($k = 1$) jet on the quantitative characteristics (i) lift, (ii) drag, and (iii) lift/drag versus (a,d,g) amplitude ratio, (b,e,f) non-dimensional frequency and (c,f,i) injection angle

frequency, and the injection angle on the lift, drag, and lift/drag, respectively, for select cases. These characteristics are important to not only gauge quantitatively the benefits of using the jet, but also give insights into the behavior of the input–output curve. The aforesaid curve behavior is crucial in analyzing the sensitivity of the parameters on the body forces on the airfoil and is thus important for system modeling and subsequent optimization.

The amplitude ratio affects the characteristics the most. This is expected as the efflux of the jet exhibits quadratic growth with an increase in the amplitude ratio. Thus, the jet adds more momentum flux to the flow and hence, can contribute to better control. The lift tends to rapidly increase (concave upward, monotonically increasing with proportional slope) as the amplitude increases [Fig. 6(i)a]. The behavior of the lift-amplitude curve is somewhat local, in that its characteristics (slope, concavity) depend on the angle and frequency chosen. As the angle of injection

increases (with constant frequency), a slope decrease is seen in Fig. 6(i)c. With an increase in the frequency (with constant angle), the curve displays increasing linear behavior. Drag remarkably decreases with an increase in the amplitude ratio [Fig. 6(ii)d]. The curve exhibits near-linear behavior, and is a strong function of the injection angle, while weakly depending on frequency. With increase in the injection angle (or frequency), the slope of the curve decreases—suggesting that the solution is not very sensitive to changes in the injection angle or frequency. The lift/drag curve depends upon the individual output parameter behavior (i.e., the lift and the drag) and thus increases rapidly as the amplitude increases, which is clear from Fig. 6(iii)g. It can be said that the curve is concave upward and monotonically increasing, more so for smaller angles of injection. The lift/drag can help one to visualize the benefits of using a synthetic jet, and hence is taken as the principal parameter of importance in the rest of the study.

The effect of frequency on the output characteristics, while minimal, cannot be overlooked. One can expect a reduction in the cycle time with an increase in frequency. Thus the frequency increase essentially means that for the same amount of time, we have more oscillations that can be used to control the flow. The effect of the frequency of the jet on the lift again depends strongly on local parameters of amplitude and angle. However, it can be said that as frequency increases, a mild increase in the lift can be expected. With an increase in angle (and at constant amplitude ratio) the curve is concave upward and monotonically decreasing, while with increasing amplitude ratio (and at constant angles) the curve becomes linear and increases monotonically. The effect of higher frequency on drag is marginally beneficial—the higher the frequency, the lesser the drag [Fig. 6(ii)e]. The response of the aforesaid curve (which is concave upward and monotonically increasing in general) with an increase in the amplitude and injection angle is different—while the former is responsible for decreasing the slope to zero, the latter increases the concavity of the curve. As can be inferred from the behavior of the lift and drag versus frequency, the lift/drag value increases with an increase in frequency, albeit very marginally [Fig. 6(iii)h]. A linear curve can be witnessed and the slope of this curve increases with either a decrease in the injection angle or an increase in the amplitude ratio.

The effect of injection angle is more straightforward. With low injection angles, the jet blows (sucks) into the fluid with the major component in the direction of the external flow. At higher angles, the jet blows (sucks) predominantly perpendicular to the boundary layer flow, probably disrupting the same. Any major disruption in the boundary layer due to transverse high momentum leads to separation, the effect of which can be seen in the characteristic values at 90° angle of injection. Thus, as expected the lift decreases with an increase in the angle of injection. The curve again shows strong dependence on the local values—stronger than the lift versus frequency curve. The curve has an inflexion point and varying local slopes, and is not discussed further for the sake of conciseness. The variation of the drag with the angle is less complex than its counterpart, and the drag increases with an increase in the injection angle almost linearly. A change in the slope from a smaller to a larger value is visible at 45°, and this is more predominant at higher amplitude ratios and lesser frequencies. Lift/drag converges at 90° for every case, irrespective of the amplitude and frequency. The curve is linear and decreasing for lower amplitudes, while at higher amplitudes it changes its behavior drastically to include an inflexion point. Frequency does not affect the lift/drag characteristics much.

Based on the above (and on the sensitivity of the parameters), curves can be fitted for this particular angle of attack (the usefulness of which was discussed earlier). The behavior of the curves for most of the input parameters shows linearity, while the other had inherent non-linearities. Hence a multi-polynomial regression fit on the data was attempted (the polynomial-type expansion was chosen due to the linearities observed earlier) and it works reasonably well, with r^2 values typically greater than 0.95. The fit equations for the lift (L), drag (D), and lift/drag (L/D) are given by (5), (6), and (7), respectively. The results for the three output parameters are given in Fig. 7.

$$L = 0.262(VR) - 0.137(F) + 0.061(F)(VR) + 0.007(\theta) - 0.006(\theta)(VR) \\ - 0.002(\theta)(F) + 0.828 + 2.687 \times 10^{-5}(\theta^2) + 0.024(F^2) + 0.059(VR^2) \tag{5}$$

$$D = -0.141(VR) - 0.056(F) + 0.013(F)(VR) - 0.002(\theta) + 0.001(\theta)(VR) \\ - 0.001(\theta)(F) + 0.387 + 2.394 \times 10^{-5}(\theta^2) + 0.009(F^2) + 0.005(VR^2) \tag{6}$$

$$\frac{L}{D} = 0.835(VR) + 0.556(F) + 1.713(F)(VR) + 0.251(\theta) - 0.336(\theta)(VR) \\ - 0.054(\theta)(F) - 1.797 + 0.002(\theta^2) + 0.224(F^2) + 5.669(VR^2) \tag{7}$$
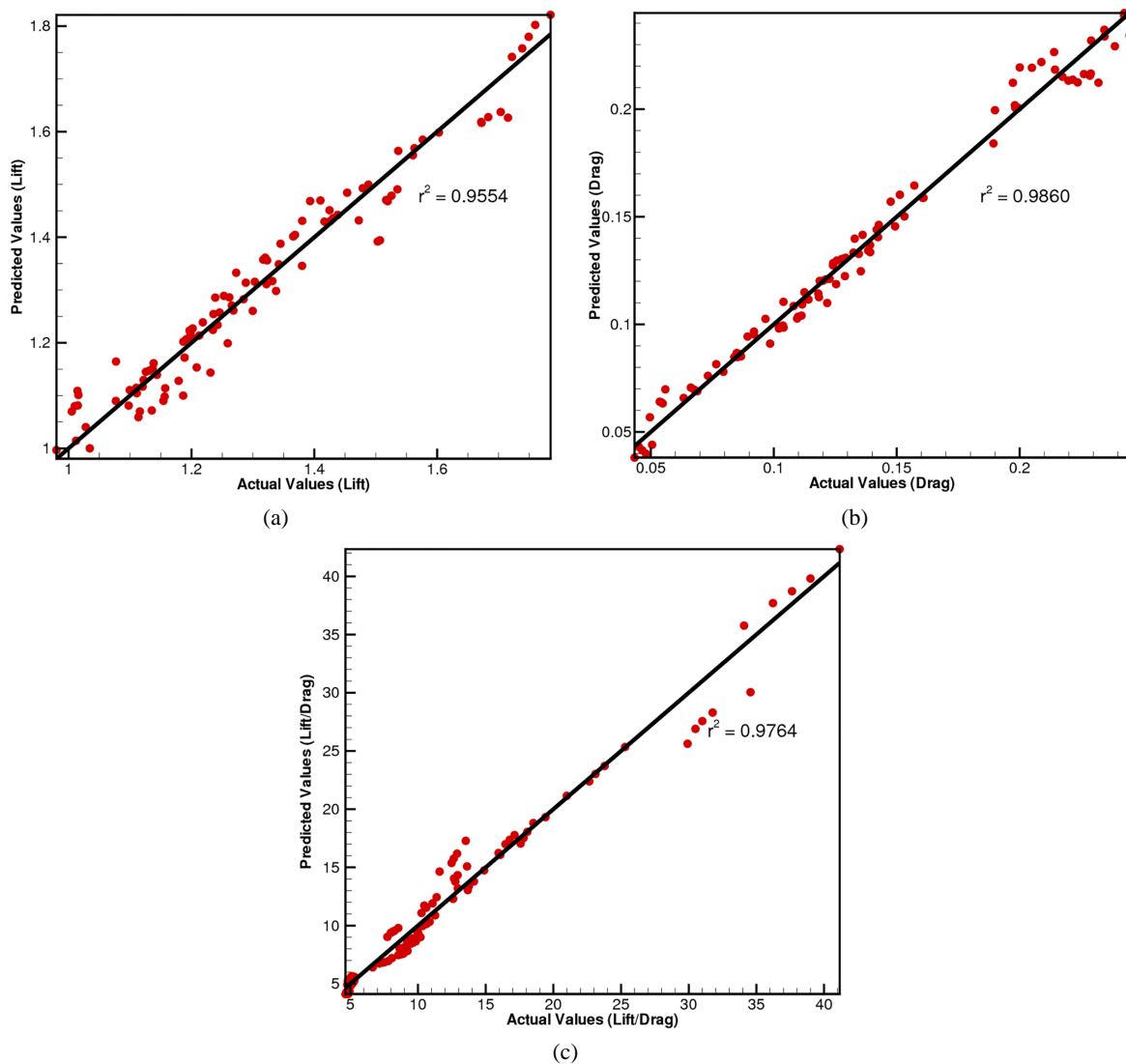
FIG. 7: Curve fits for the (a) lift, (b) drag, and (c) lift/drag

3.2 Flow Physics

Furthering the above discussions on the benefits of flow control using synthetic jets, it is important that one understands the phenomenon that elicits the control response. This can be understood through qualitative arguments made by comparing the flow streamlines, vorticity contours, and the airfoil wall pressure coefficient. Furthermore, the controlled flow exhibits different flow structures for a different set of parameters, making it worthwhile to look at these structures for a range of parameters. Figure 8 gives the qualitative features for the baseline flow at 20° angle of attack, which can be used to delineate the cause of the control.

A particular case of {0.6446/30°/1.5/1} (that corresponds to a non-dimensional frequency of 0.6446, 30° angle of injection, amplitude ratio of 1.5, and a suction ratio of 1) is used to delineate the associated physics. The synthetic jets adds momentum flux and vorticity flux to the external flow, without any mass flux addition. This momentum flux is instrumental in separation control, which is done by adding high-momentum fluid to the boundary layer during the blowing stroke [Fig. 9(i)b] and by removing the proximal low-momentum fluid during the suction stroke [Fig. 9(i)d],
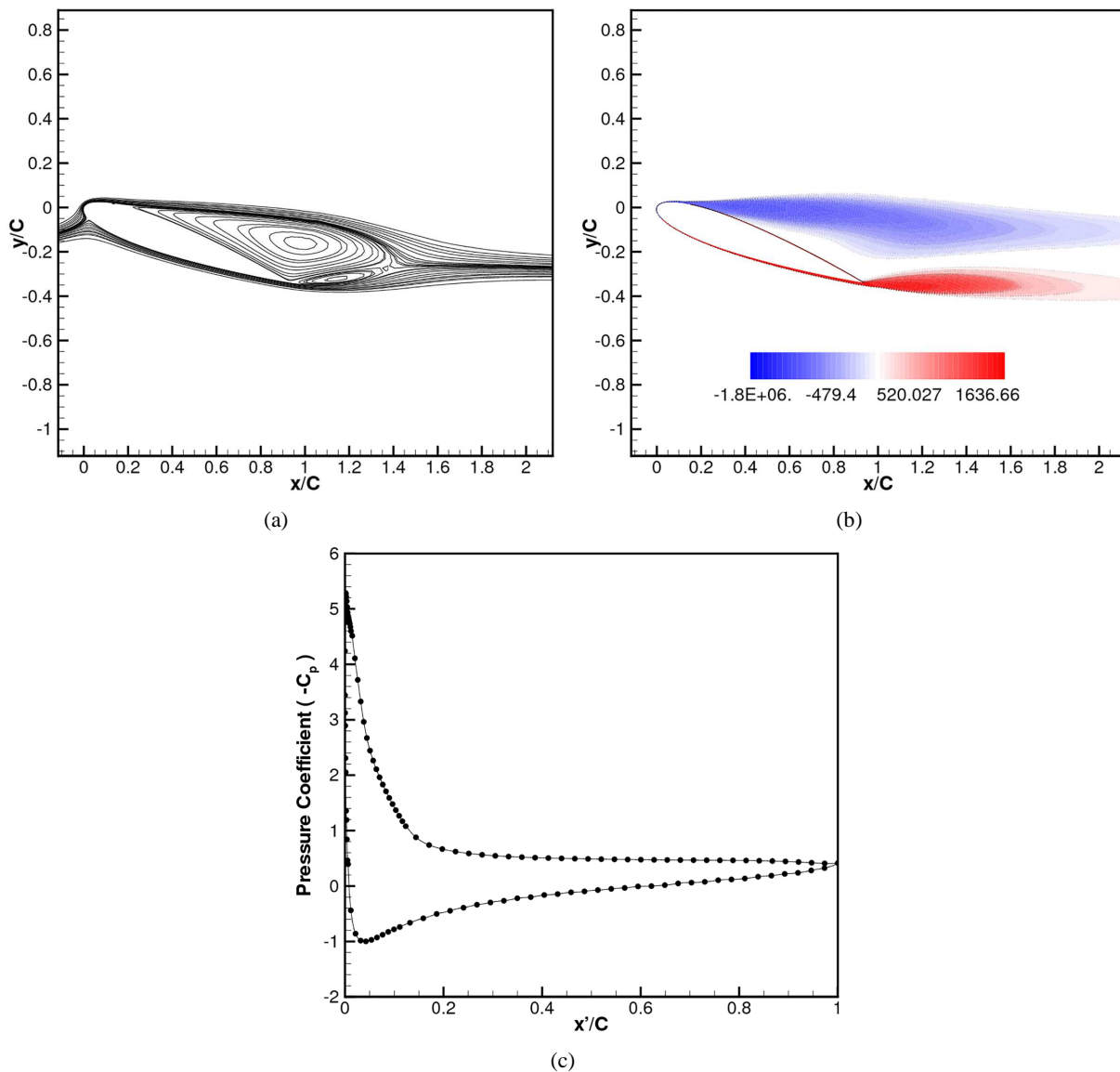
(a)

(b)

(c)

FIG. 8: Qualitative flow structures for the uncontrolled case at 20° AoA: (a) Streamfunction, (b) vorticity, and (c) wall pressure coefficient $(-C_p)$

leading to stifled separation across the phases, as can be seen in Fig. 9(i). A synthetic jet in a quiescent flow is characterized by the vortex rings (which are observed as a pair of counter-rotating vortices in 2D and which is essentially a manifestation of the vorticity flux) emanating into the surroundings, which carries the aforesaid momentum flux along with it. On observing the vorticity contour diagrams [Fig. 9(ii)], it can be said that the control aspect involves the convective transport of these generated vortices downstream. The vortices are generated during the blowing stroke [Fig. 9(ii)b], while the suction stroke is marked by coalescence of these vortices with the external flow [Fig. 9(ii)d], which is achieved by bringing higher-momentum fluid of the external flow to mix with these vortices [Fig. 9(ii)d]. While the strength of the anticlockwise vortex (from the left edge of the synthetic jet wall) is diminished, the other vortex is sustained and can be seen as a thick blob of vorticity. The vortex becomes physically significant in the suction stroke, after traveling a particular distance downstream due to reasons mentioned before. A typical vortex
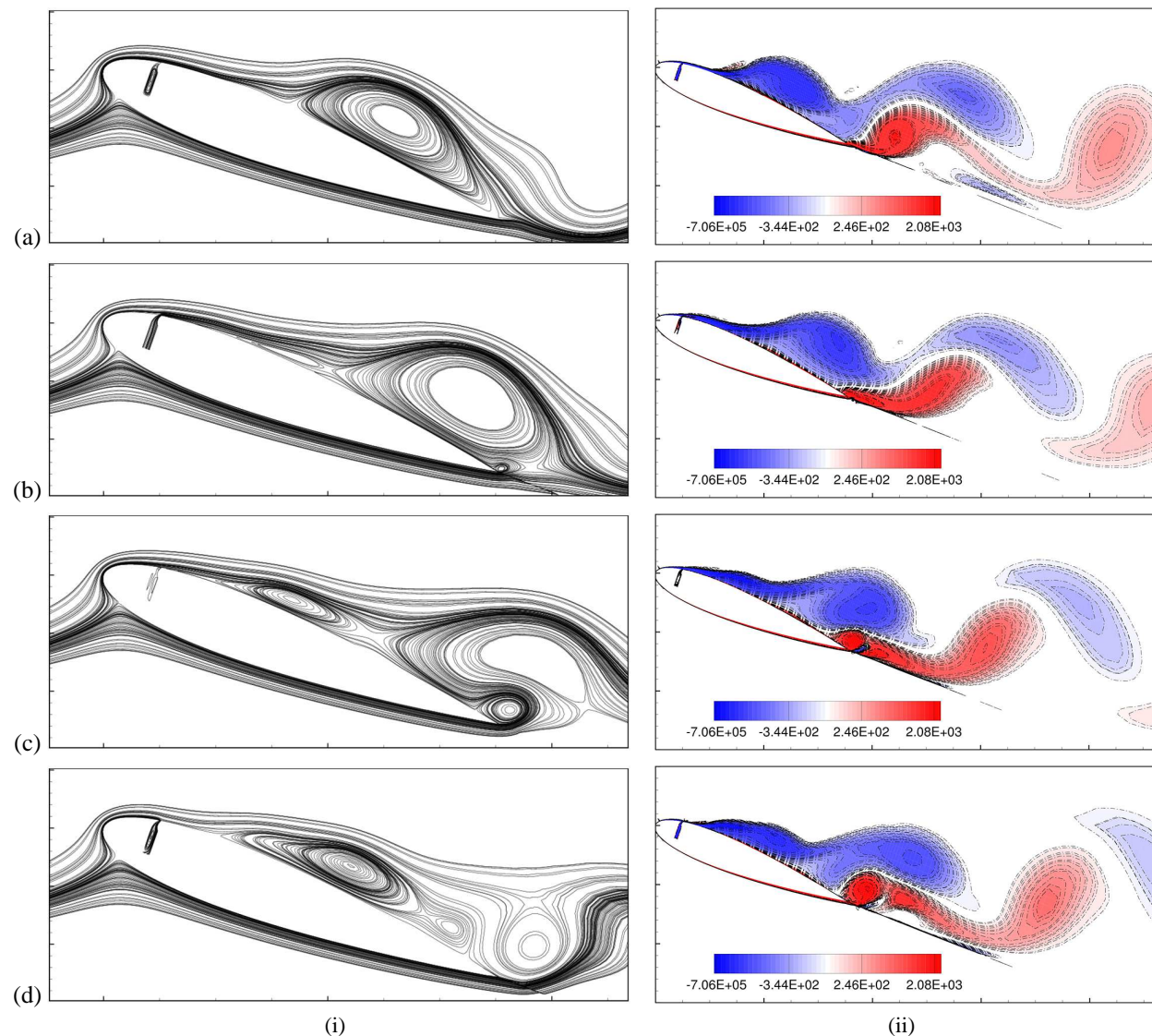
FIG. 9: (i) Streamline and (ii) vorticity contours for the controlled flow {0.6446/30°/1.5/1} at (a) $\Phi = 0°$, (b) $\Phi = 90°$, (c) $\Phi = 180°$, and (d) $\Phi = 270°$. Phase (Φ) is defined as seen in Fig. 5

shedding pattern is then presented, while there was none in the baseline case. The vortex shedding causes a decrease in the wake width subsequently, thereby decreasing drag. The above explanation is bolstered by observing the phase (ϕ)-averaged pressure coefficient plots (Fig. 10). The discontinuity in the pressure coefficient plot of the aerofoil wall [Figs. 10(b) and 10(d)] is because of the presence of the jet at 12% chord length. It can be seen that the vortex emanating from the synthetic jet contributes to a low-pressure "wave" [Fig. 10(b)]. This wave travels downstream from its point of origin [marked in Fig. 10(c)], much like the vortex, and causes an increase in the area bound within the pressure coefficient curve (thus increasing the lift). This "wave" is caused due to high magnitudes of differential pressure generated by the jet at different phases of the operation cycle. For example, suction causes local decrease in pressure on the suction side before the jet and local increase in pressure after the jet [Fig. 10(d)], due to appropriate deflection of streamlines (and thus fluid velocity), which causes a trough. The same applies for blowing [Fig. 10(b)], which creates a crest. As stated in a previous work (You and Moin, 2008), the suction stroke removes the low-momentum
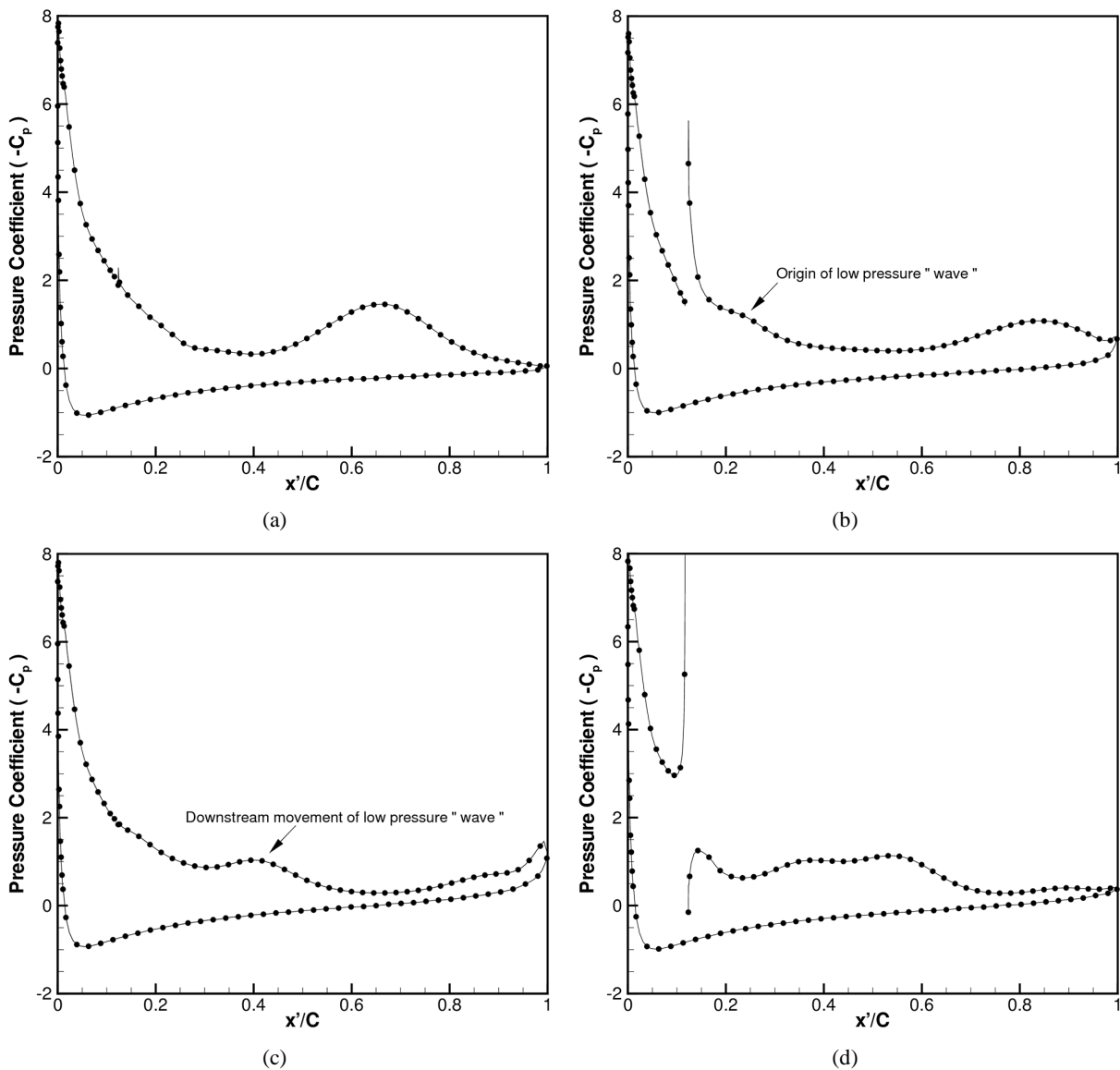
FIG. 10: Wall pressure coefficient $(-C_p)$ for the controlled flow $\{0.6446/30°/1.5/1\}$ at (a) $\Phi = 0°$, (b) $\Phi = 90°$, (c) $\Phi = 180°$, and (d) $\Phi = 270°$

fluid in the upstream and the blowing energizes the downstream by adding momentum to the same. While the above explanation summarizes the basis for the controlling aspect of the flow, differences creep in based on the parameters selected.

Upon changing the jet parameters, several observations can be made. The amplitude changes the momentum flux and significantly affects the external flow. This means that the vortices generated are stronger and can affect the flow significantly. The impact of this is felt when the leading edge type of the separation bubble of the baseline case is converted to a pre-stall trailing edge type separation at higher amplitudes. Frequency affects the number of vortices being shed per unit time, and thus leads to a different number of vortices/waves/separation bubbles as observed in the qualitative figures. The angle of injection, as explained earlier, changes the transverse velocity component into the boundary layer and causes reattachment (or) separation. Additionally, the generated vortex manifests itself and

later sheds at different spatio-temporal values, based on the flow parameters selected. The same can be said for the amplitude, frequency, and location of the generated pressure "waves." Figures 11, 12, and 13 show the changes in the qualitative flow structures based on the parameters selected. The results shown are not exhaustive, but are representative of the findings.

Figures 11(i), 12(i), and 13(i) indicate the results of a change in the amplitude ratio from the controlled case shown earlier. One can see that the body appears more streamlined and thinner than the external flow from Fig. 11(i), and the separation is effectively controlled. Also, as the amplitude ratio is high, the fluid elements having intense vorticity have higher velocities, and convect downstream with the same. Thus the diffusion of these vortices into the wake takes longer due to the high velocity. Thus the vortices appear stretched, and hence take more time to expand and dissipate out [Fig. 12(i)]. The pressure coefficient plots do not show variation across phase [Fig. 13(i)]. This is expected as the separation in this case is delayed, appears steady [Fig. 11(i)], and the vortex essentially spans the downstream distance quickly.

The jet with a change in the frequency from the controlled case presented in Figs. 9 and 10 behaves as shown in Figs. 11(ii), 12(ii), and 13(ii). The body appears more bluff to the external flow but is locally thin at some locations [Fig. 11(ii)d]. As expected, the frequency changes the number of vortices generated per unit time and more such vortices are generated at higher frequencies. The shed vortices comparatively travel lesser distance downstream before the next cycle, and so any particular case captures more vortices in the contour diagram [Fig. 12(ii)]. This also explains why the pressure coefficient diagram [Fig. 13(ii)] across the phases appears to have multiple local crests and troughs—i.e., the vortices shed in the previous cycle impact the physics of the subsequent one. The same can be said upon observing the streamlines of Fig. 11(ii).

A change in the angle of inclination changes the components of velocity and the flow structures are a direct result of the same. This can be seen in Figs. 11(iii), 12(iii), and 13(iii). By blowing perpendicularly into the boundary layer the separation bubble size seems to have increased [Fig. 11(iii)a] locally. The vortices also diffuse quicker and contribute to a bigger wake as they drift apart from the wall at a faster rate [Fig. 12(iii)]. The size of the vortex at
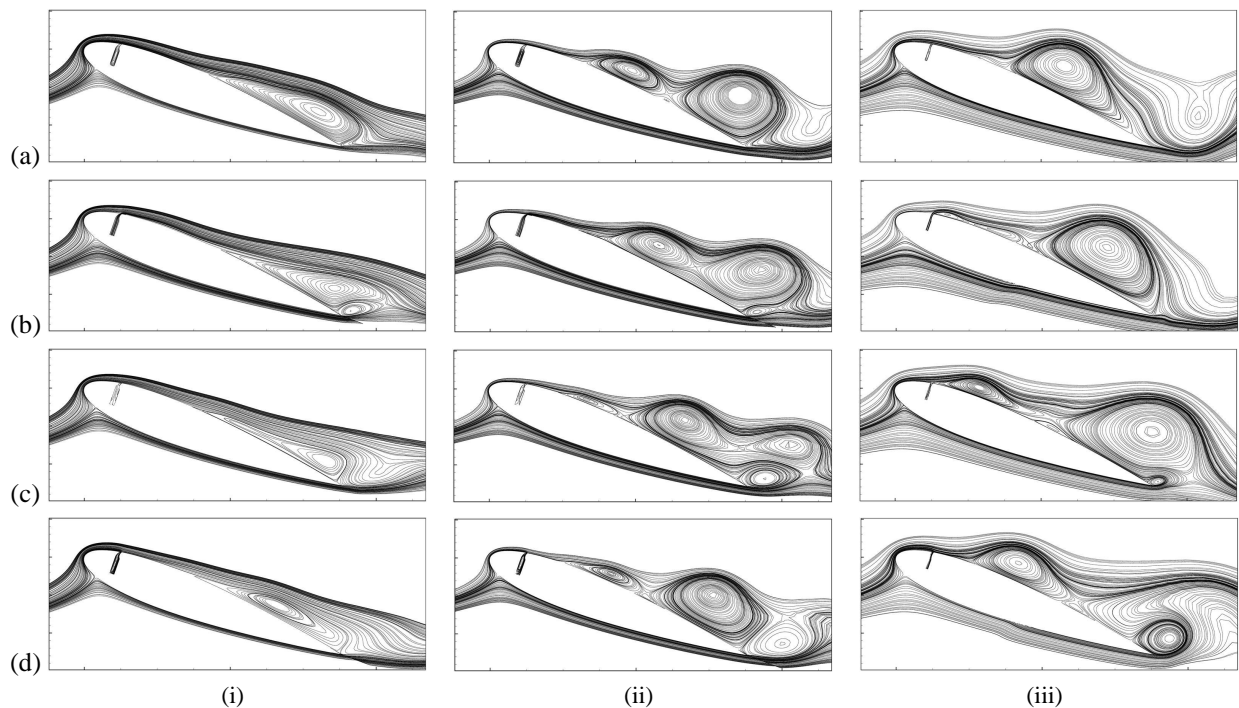

FIG. 11: Streamline contours for the controlled flow cases (i) $\{0.6446/30°/2.25/1\}$, (ii) $\{1.1281/30°/1.5/1\}$, (iii) $\{0.6446/60°/1.5/1\}$ at (a) $\Phi = 0°$, (b) $\Phi = 90°$, (c) $\Phi = 180°$, and (d) $\Phi = 270°$
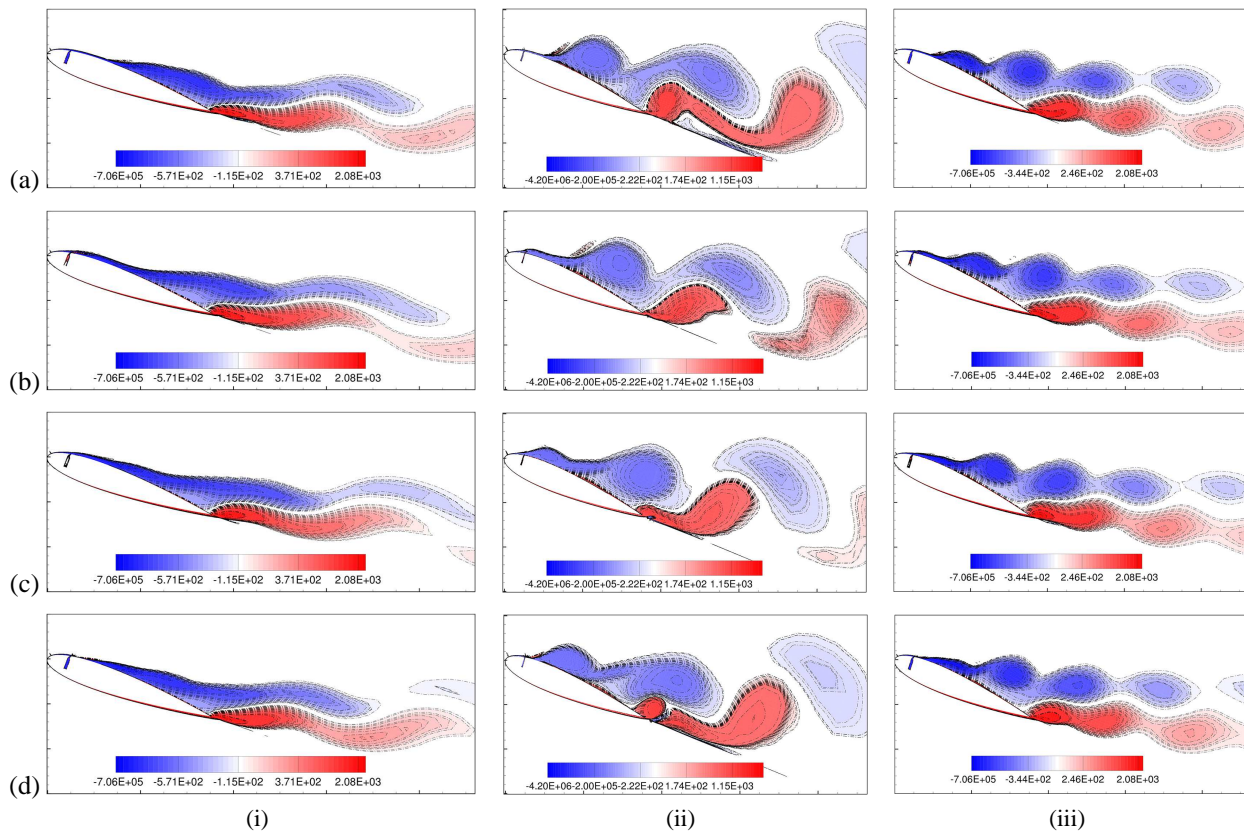
FIG. 12: Vorticity contours for the controlled flow cases (i) $\{0.6446/30°/2.25/1\}$, (ii) $\{1.1281/30°/1.5/1\}$, (iii) $\{0.6446/60°/1.5/1\}$ at (a) $\Phi = 0°$, (b) $\Phi = 90°$, (c) $\Phi = 180°$, and (d) $\Phi = 270°$

any phase is also significantly bigger. As seen in Fig. 13(iii), the pressure "wave" is now sharper in its form, but unfortunately the troughs dig too deep in the area occupied by the plot. Thus the net area occupied is lesser, and the flow separates sooner, leading to the conclusion that a smaller angle is preferable for jet operation.

While load control and separation control in this case (20° angle of attack) are inherently linked due to the baseline flow, it is possible to identify certain characteristics that indicate the degree of separation control that are achieved by the input parameters. Two such characteristics are discussed here: the shape factor (versus phase) immediately after the jet (based on wall normal velocity profile at a section that begins on the wall at 16% chord length from the leading edge) and the phase-averaged wake characteristics at a downstream location (at a section perpendicular to the chord line at 120% chord length from the leading edge). The shape factor (H) is the ratio of displacement thickness (δ^*) to the momentum thickness (δ^{**}) and higher magnitude of the same indicate that the flow is more likely to separate (thus the location of measurement is valid and meaningful), the reason for which can be easily understood by looking at the definition of δ^* and δ^{**}. Figure 14 is representative of the same and shows the most important cases. Figure 14(a) indicates that the separation control strategy is indeed effective. Furthermore, it also shows that the latter half (suction) of the cycle contributes to a better separation control than the former half (blowing). Even for the controlled cases, one can witness that at $\emptyset \sim 180°$, the separation characteristics are undesirable. Higher amplitude ratios lead to better separation control as expected, but so does higher frequency! Some values corresponding to the case $\{0.6446/60°/1.5/1\}$ are not shown, as the flow is separated there. The wake width and centerline velocity lag significantly affects the theoretical drag calculations, and also indicate the performance of the jet. The effect of amplitude, frequency, and injection angle on the wake characteristics follows from the discussions made previously: with higher amplitude, lesser injection angle cases perform better [Fig. 14(b)].
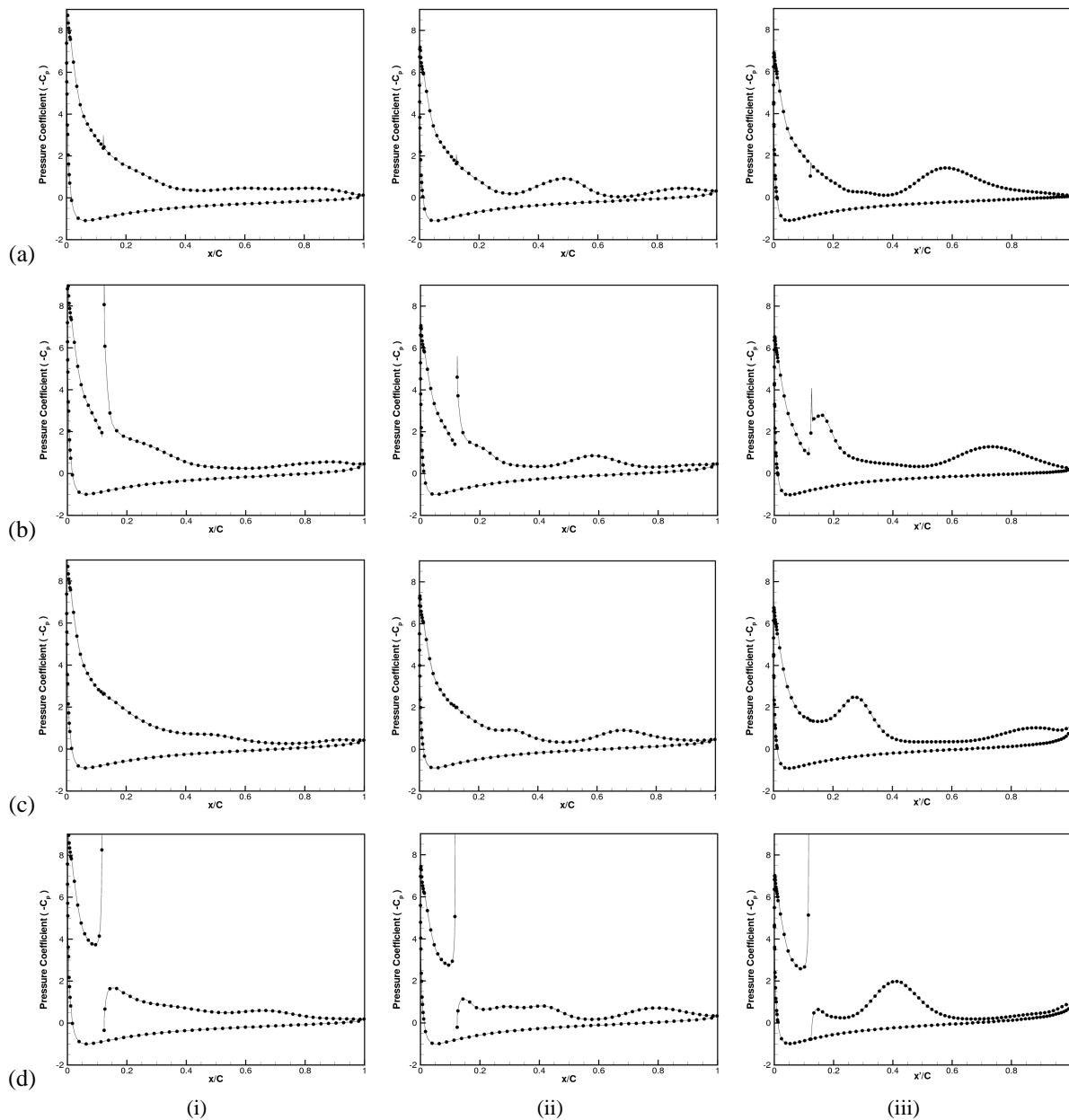
FIG. 13: Wall pressure coefficient $(-C_p)$ for the controlled flow cases (i) {0.6446/30°/2.25/1}, (ii) {1.1281/30°/1.5/1}, (iii) {0.6446/60°/1.5/1} at (a) $\Phi = 0°$, (b) $\Phi = 90°$, (c) $\Phi = 180°$, and (d) $\Phi = 270°$

3.3 Time Modulation of the Synthetic Jet

An interpretation of the load (Fig. 5) and shape factor [Fig. 14(a)] plots seems to indicate that more benefits can be reaped by controlling the time duration of suction and blowing. A simple case of the same was studied earlier (Feng and Wang, 2014). There are, according to the authors' knowledge, no studies on its application to flow control over aerofoils. Physically speaking, this can be achieved in the present case by using piston cylinders attached to quick return mechanisms. The controlling parameter in this case will be the ratio of suction and blowing time within a time
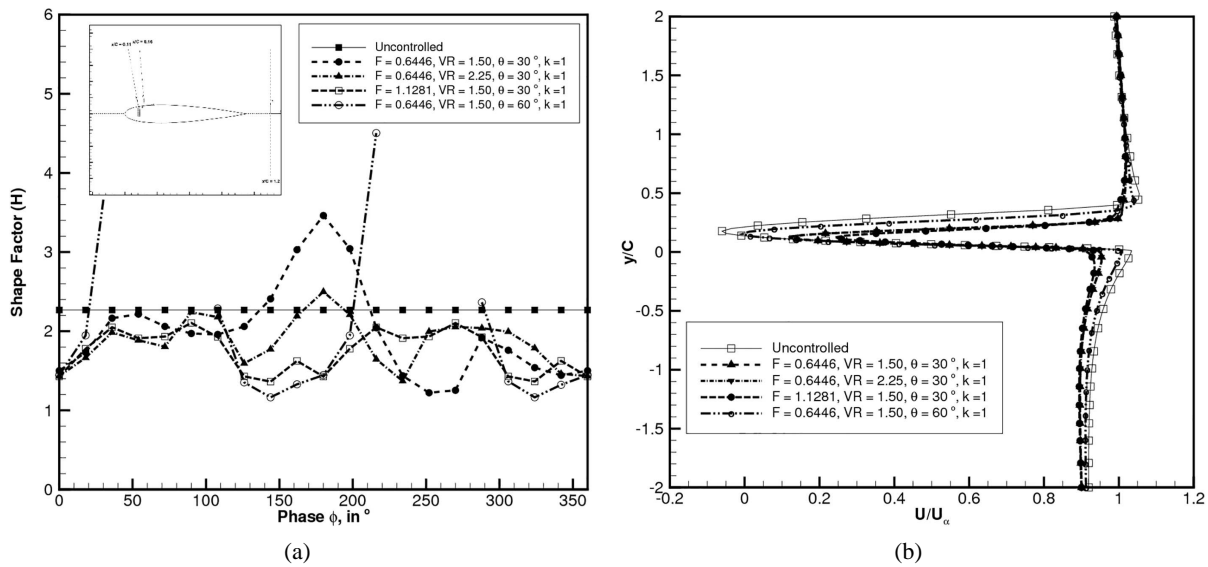
FIG. 14: (a) Shape factor measured at x/C = 0.16 and (b) wake measured at x/C = 1.2 for some controlled cases

period defined by the parameter k. As with the synthetic jet that was modeled using a simple sinusoidal function, the time-modulated synthetic jet can also be modeled along similar lines, although the profile is now piecewise to satisfy the various conditions imposed (continuity and mass flux conservation, etc.). The time period T is based on the frequency (f). A suitable profile for initial analysis (although the derivatives are not continuous) is given below, such that the maximum amplitude in the cycle corresponds to the amplitude ratio similar to the one considered earlier:

$$V_{jet} = \begin{cases} A_b \sin\left(2\pi f_b t\right), & 0 \leq t \leq T_b \\ A_s \sin\left(2\pi f_s \left[t + \dfrac{(k-1)\,T}{(k+1)}\right]\right), & T_b \leq t \leq T \end{cases}$$

$$T_b = \frac{T}{k+1}$$

$$f_b = \frac{k+1}{2T}$$

$$f_s = \frac{k+1}{2kT}$$

$$A = \begin{cases} A_s = A_p, & A_b = \dfrac{f_b A_s}{f_s}, & k \leq 1 \\ A_b = A_p, & A_s = \dfrac{f_s A_b}{f_b}, & k \geq 1 \end{cases}$$

(8)

Figure 15 indicates the quantitative results of applying the time-modulated synthetic jet on the airfoil, for varying amplitudes (as this affected the curves earlier the most) at a non-dimensional frequency of 1.6117 and 30° angle of injection. It can be clearly seen that at lower suction ratios ($k < 1$) the performance is abysmal throughout the range for all the characteristics, while at higher suction ratios ($k > 1$) there is marginal improvement in lift for practically achievable amplitudes. This is however offset by a marginal increase in drag as well. An overall marginal improvement in the lift/drag values can be seen.

Figures 16, 17, and 18 give the qualitative structures of the time-modulated flow. The phase used to describe the modulated flow corresponds to the phase of the unmodulated profile. This is because the modulated profile consists of two different functions, and the term phase loses meaning. For example, while 90° implies a maximum in blowing for
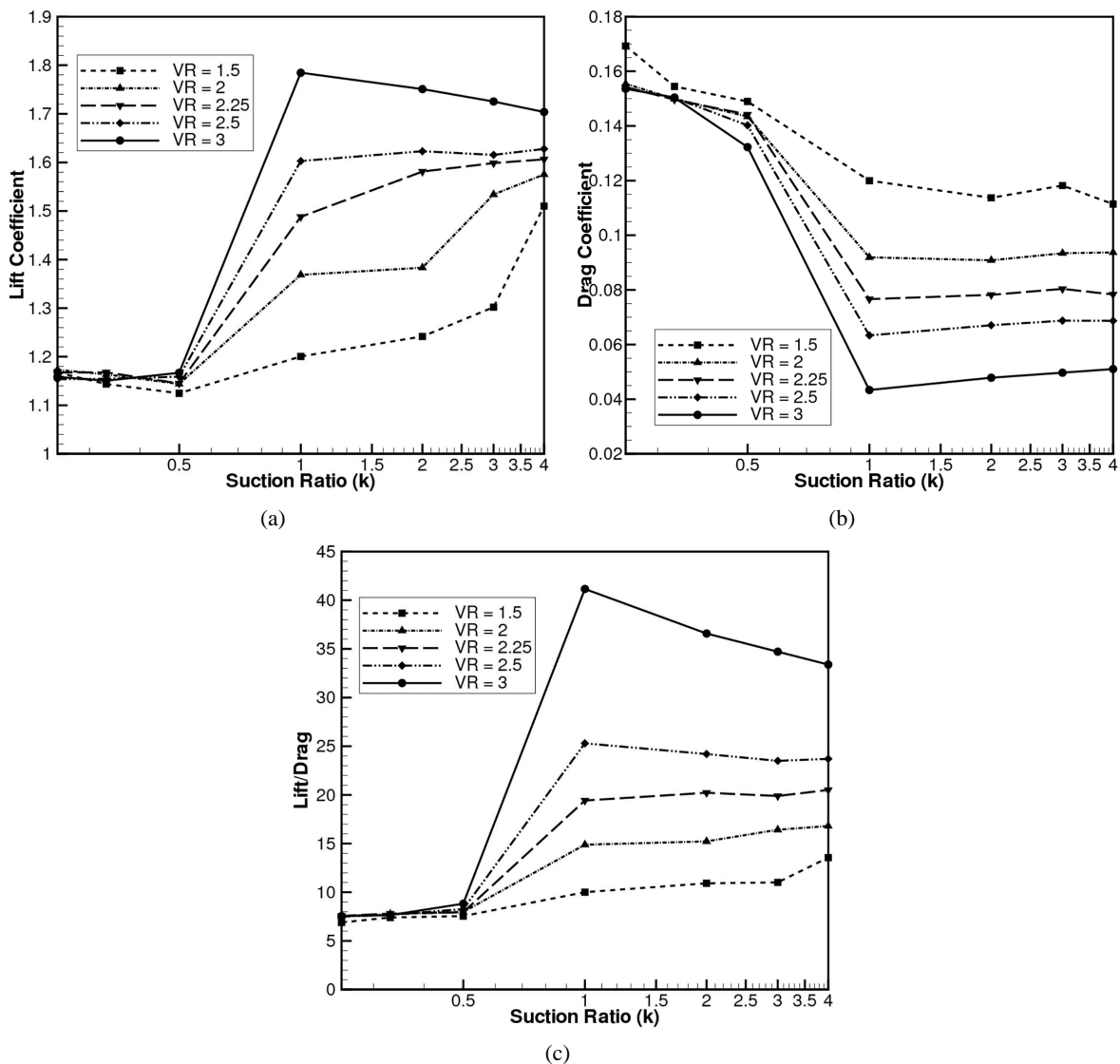
FIG. 15: Effect of the suction ratio (k) on the (a) lift, (b) drag, and (c) lift/drag, for varying amplitude ratios

the unmodulated profile, it does not imply the same for the modulated profile. The flow structures for all cases in the lower suction ratios are of a similar type. This is true for high-suction ratio flows as well. Thus a comparison between low-suction ratio, unmodulated ($k = 1$), and high-suction ratio flows is adequate. Low-suction ratio flows appear bluffer to the flow with increased local thickness, as can be seen from Fig. 16(i). The vorticity pattern [Fig. 17(i)] is akin to a flow with lower convective motion [with respect to the unmodulated case, Fig. 17(ii)] than its high-suction counterpart, which is expected as fluid is injected with lesser amplitude, but over a prolonged period. The pressure coefficient curve [Fig. 18(i)] indicates major fluctuations (due to stronger suction amplitude, which creates troughs with higher magnitudes) and this causes a net decrease in the occupied area. Meanwhile high-suction ratio flows are more streamlined [Fig. 16(iii)] and exhibit vortex shedding [Fig. 17(iii)] that can clearly be distinguished. The pressure coefficient curves [Fig. 18(iii)] are comparable to the unmodulated flow except for a slight increase in the occupied area due to the local pressure decrease (crest) during the blowing stroke (which is not captured in the given figures).
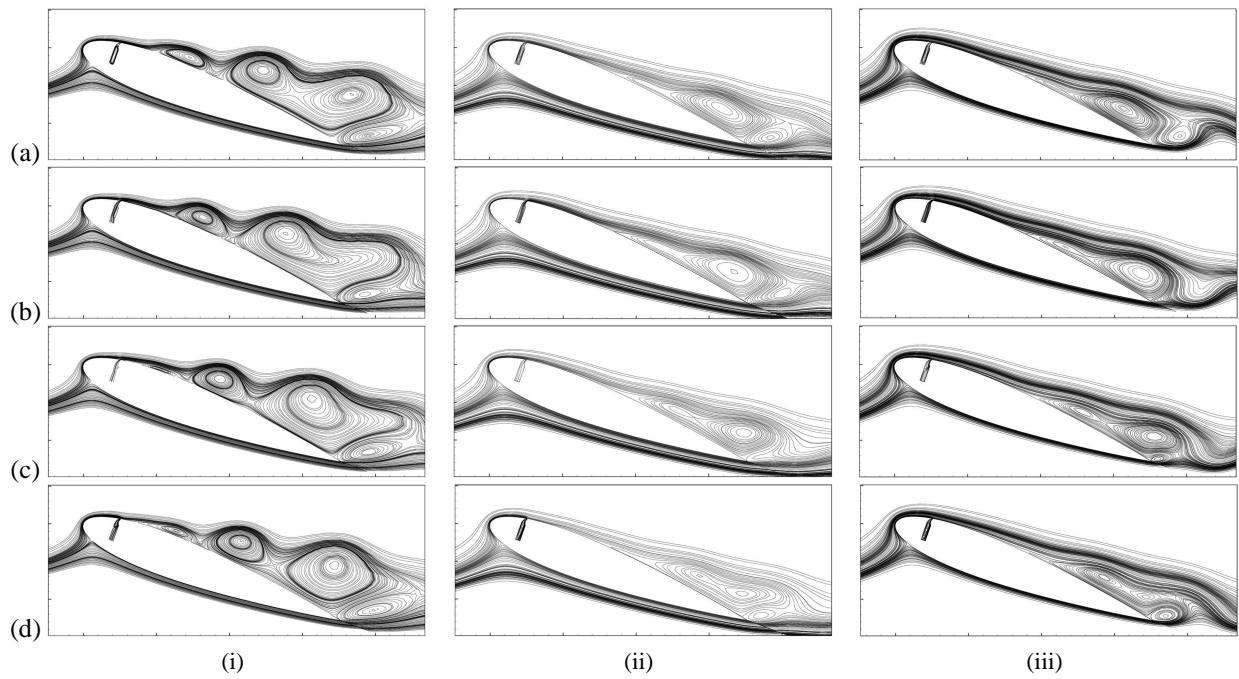
FIG. 16: Streamline contours for the controlled flow cases (i) {1.6117/30°/2.25/0.5}, (ii) {1.6117/30°/2.25/1}, (iii) {1.6117/30°/2.25/2} at (a) $\Phi = 0°$, (b) $\Phi = 90°$, (c) $\Phi = 180°$, and (d) $\Phi = 270°$
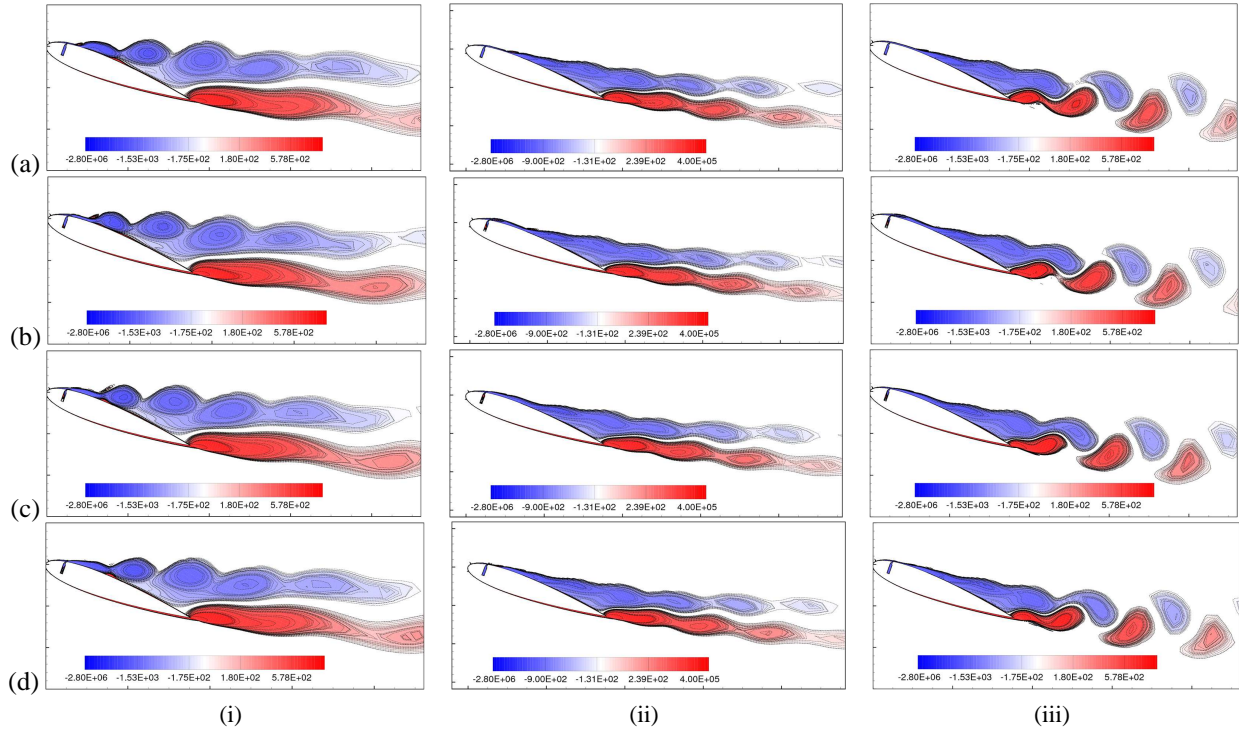

FIG. 17: Vorticity contours for the controlled flow cases (i) {1.6117/30°/2.25/0.5}, (ii) {1.6117/30°/2.25/1}, (iii) {1.6117/30°/2.25/2} at (a) $\Phi = 0°$, (b) $\Phi = 90°$, (c) $\Phi = 180°$, and (d) $\Phi = 270°$
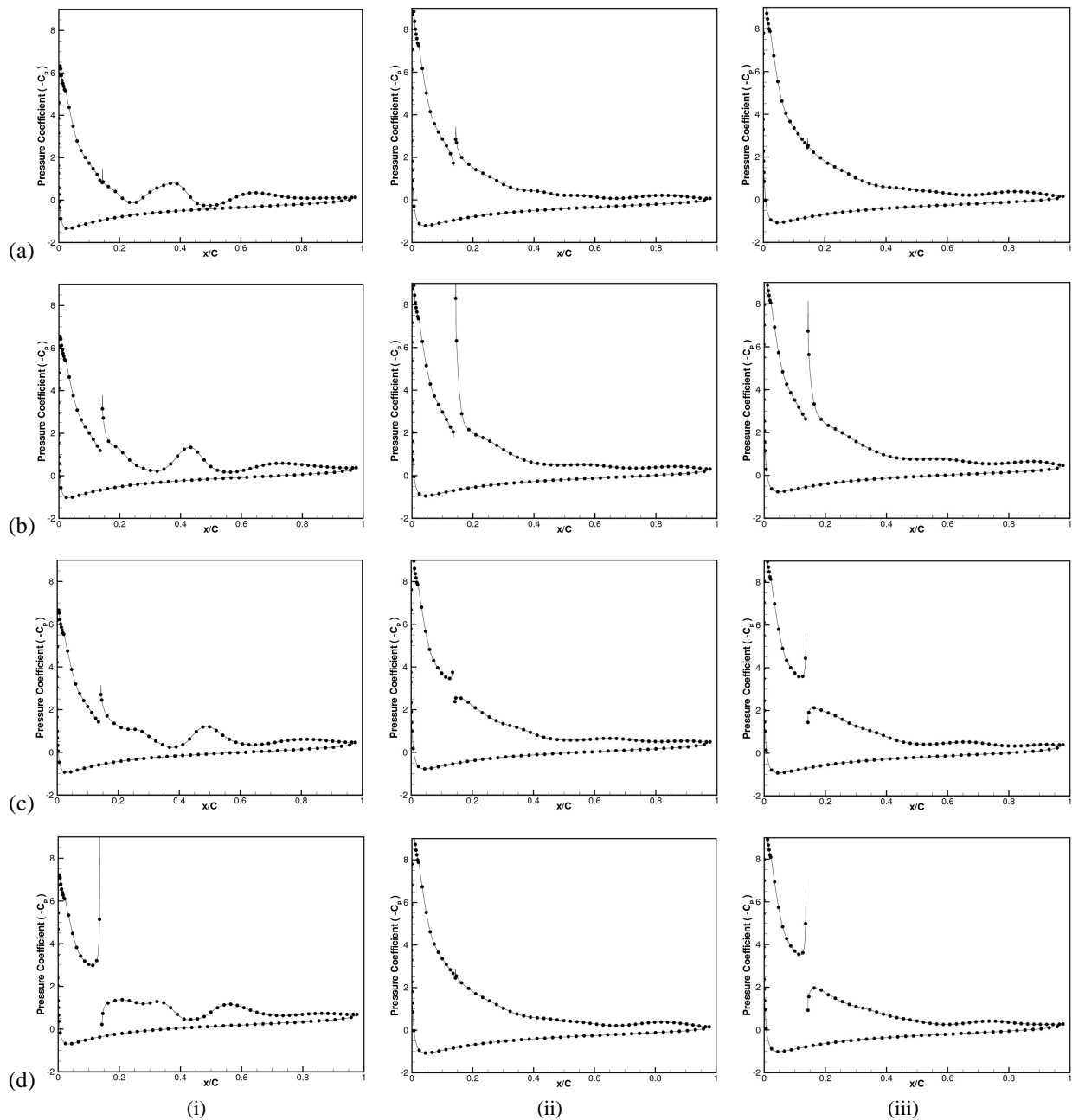
FIG. 18: Wall pressure coefficient $(-C_p)$ for the controlled flow cases (i) $\{1.6117/30°/2.25/0.5\}$, (ii) $\{1.6117/30°/2.25/1\}$, (iii) $\{1.6117/30°/2.25/2\}$ at (a) $\Phi = 0°$, (b) $\Phi = 90°$, (c) $\Phi = 180°$, and (d) $\Phi = 270°$

Figure 19 similarly gives an insight into the shape factor and wake width. As can be seen in Fig. 19(a), the separation characteristic is the best for the high-suction ratio flow, while the unmodulated flows offer a marginally reduced performance. The low-suction ratio flows, as expected, do not perform well. The same can be observed in the wake characteristics [Fig. 19(b)], wherein the wake of the low-suction ratios is wider, and the centerline velocity lag is more pronounced—thus leading to more drag.
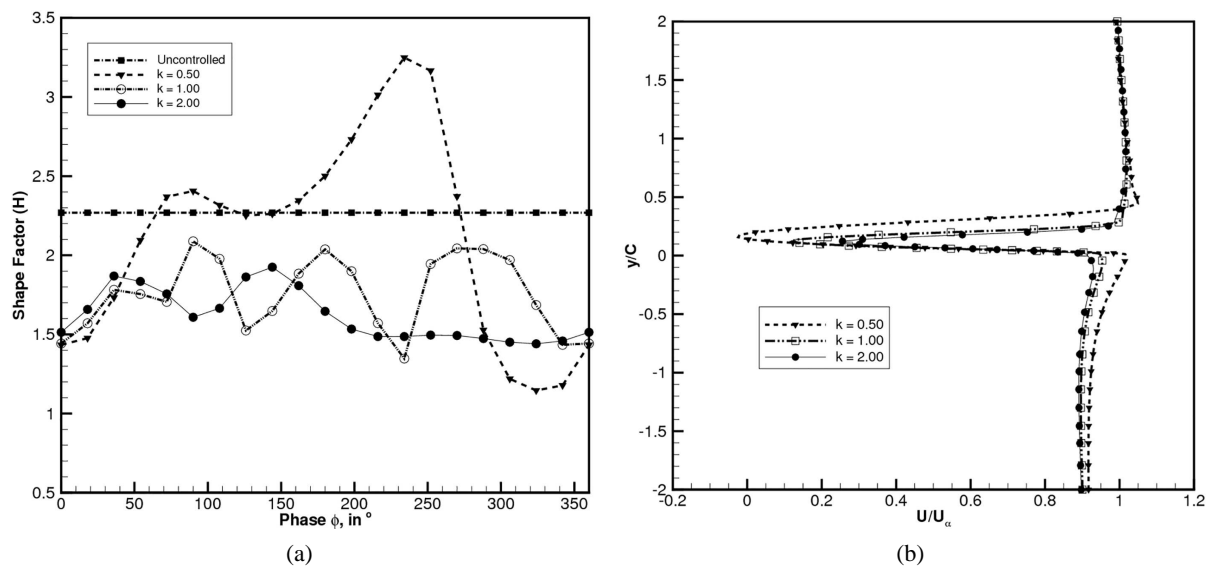
FIG. 19: (a) Shape factor measured at x/C = 0.16 and (b) wake measured at x/C = 1.2 for controlled cases with varying suction ratios

4. CONCLUSIONS

In the present work, a RANS simulation of a turbulent separated flow over a plain and synthetic jet embedded NACA 0015 airfoil was performed. The effectiveness of the synthetic jet, as listed in previous studies, was once again confirmed. A detailed parametric study of the conventional synthetic jet parameters was carried out. Its effect on the lift, drag, and lift/drag values of the airfoil were recorded and analysed. A curve-fit model for the same was presented, which can be used for sensitivity and optimization studies. For practically achievable actuators, the free-stream lift is maximum at higher amplitudes, lower injection angles, and higher frequencies and increases by as much as 36%. Detailed flow structures were presented and the control response could be explained. By bringing in higher momentum fluid into the near-wall flow (and thus contributing to pressure "waves" that convect downstream), the synthetic jet engenders flow control. Separation delay for the actuator was also studied and both the suction and blowing phases were found to be beneficial. On the basis of the aforementioned studies, a new parameter for eliciting good control response—the suction ratio—was explored. Investigations into the same revealed that the performance enhancement from the same at its optimal value is only very marginal: a 5% increase in lift/drag. This does not justify installing a quick return mechanism for this particular scale of operation, although synthetic jets based on piezoelectric actuators can be quickly tuned to the same and hence can exploit the said benefits. The separation performance of the time modulated jet is also looked into. Future studies into the interaction between multiple jets, development of a wing-control mechanism, and control-related heat transfer phenomenon can be done with the present study acting as a guide.

REFERENCES

Akcayoz, E. and Tuncer, I.H., Numerical investigation of flow control over an airfoil using synthetic jets and its optimization, *Ankara International Aerospace Conf.*, Ankara, Turkey, August 17–19, 2009.

Collis, S.S., Joslin, R.D., Seifert, A., and Theofilis, V., Issues in active flow control: Theory, control, simulation, and experiment, *Prog. Aerosp. Sci.*, vol. **40**, no. 2, pp. 237–289, 2004.

Dannenberg, R.E. and Weiberg, J.A., Section characteristics of a 10.5-percent-thick airfoil with area suction as affected by chordwise distribution of permeability, NASA Tech. Rep.; NACA TN-2847, National Advisory Committee for Aeronautics, Ames Aeronautical Lab, Moffett Field, CA, 1952.

De Giorgi, M.G., De Luca, C.G., Ficarella, A., and Marra, F., Comparison between synthetic jets and continuous jets for active flow control: Application on a NACA 0015 and a compressor stator cascade, *Aerosp. Sci. Technol.*, vol. **43**, pp. 256–280, 2015.

Donovan, J., Kral, L., and Cary, A., Active flow control applied to an airfoil, *36th AIAA Aerospace Sciences Meeting and Exhibit*, Reno, NV, January 12–15, 1998.

Drela, M., XFOIL: An analysis and design system for low reynolds number airfoils, in *Low Reynolds Number Aerodynamics*, Berlin: Springer, pp. 1–12, 1989.

Duvigneau, R. and Visonneau, M., Simulation and optimization of stall control for an airfoil with synthetic jet, *Aerosp. Sci. Technol.*, vol. **10**, no. 4, pp. 279–287, 2006.

Feng, L.H. and Wang, J.J., The virtual aeroshaping enhancement by synthetic jets with variable suction and blowing cycles, *Phys. Fluids*, vol. **26**, no. 1, 014105, 2014.

Gilarranz, J.L., Traub, L.W., and Rediniotis, O.K., A new class of synthetic jet actuators-Part II: Application to flow separation control, *ASME J. Fluids Eng.*, vol. **127**, no. 2, pp. 377–387, 2005.

Glezer, A. and Amitay, M., Synthetic jets, *Annu. Rev. Fluid Mech.*, vol. **34**, no. 1, pp. 503–529, 2002.

Goodfellow, S.D., Yarusevych, S., and Sullivan, P.E., Momentum coefficient as a parameter for aerodynamic flow control with synthetic jets, *AIAA J.*, vol. **51**, no. 3, pp. 623–631, 2012.

Iaccarino, G., Marongiu, C., Catalano, P., and Amato, M., RANS modeling and simulations of synthetic jets, *2nd AIAA Flow Control Conf.,* Portland, OR, June 28–July 1, 2004.

Jahanmiri, M., Active flow control: A review, Göteborg, Sweden, Chalmers University of Technology, Research rep. 2010:12, 2010.

Jirásek, A., Vortex-generator model and its application to flow control, *J. Aircr.*, vol. **42**, no. 6, pp. 1486–1491, 2005.

Kitsios, V., Kotapati, B., Mittal, R., Ooi, A., Soria, J., and You, D., Numerical simulation of lift enhancement on a NACA 0015 airfoil using ZNMF jets, *Proc. of the Summer Program, Center for Turbulence Research*, Stanford University/NASA, CA, USA, pp. 457–468, July 9–August 4, 2006.

Lasagna, D., Donelli, S., De Gregorio, F., Orazi, M., and Iuso, G., Separation delay on thick airfoil using multiple synthetic jets, *XXI Congresso Associazione Italiana di Meccanica Teorica e Applicata Conf.*, Torino, Italy, September 17–20, 2013.

McAlister, K.W. and Takahashi, R.K., NACA 0015 wing pressure and trailing vortex measurements, NASA Tech. Rep., NASA-A-91056, National Advisory Committee for Aeronautics, Ames Aeronautical Lab., Moffett Field, CA, 1991.

McCormick, D., Boundary layer separation control with directed synthetic jets, *38th Aerospace Sciences Meeting and Exhibit*, Reno, NV, January 10–13, 2000.

Mittal, R. and Rampunggoon, P., On the virtual aeroshaping effect of synthetic jets, *Phys. Fluids*, vol. **14**, no. 4, pp. 1533–1536, 2002.

Okada, K., Fujii, K., and Miyaji, K., Computational study of frequency and amplitude effects on separation flow control with the synthetic jet, *ASME Int. Mech. Engineering Congress and Exposition; Heat Transfer, Fluids, and Thermal Systems, Parts A, B, and C*, Lake Buena Vista, FL, pp. 289–298, November 13–19, 2009.

Raju, R., Mittal, R., and Cattafesta, L., Dynamics of airfoil separation control using zero-net mass-flux forcing, *AIAA J.*, vol. **46**, no. 12, pp. 3103–3115, 2008.

Raju, R., Aram, E., Mittal, R., and Cattafesta, L., Simple models of zero-net mass-flux jets for flow control simulations, *Int. J. Flow Control*, vol. **1**, no. 3, pp. 179–197, 2009.

Ravindran, S.S., Active control of flow separation over an airfoil, NASA Tech. Rep. RM-1999-209838, 1999.

Spalart, P. and Allmaras, S., A one-equation turbulence model for aerodynamic flows, *30th Aerospace Sciences Meeting and Exhibit*, Seattle, WA, January 6–9, 1992.

You, D. and Moin, P., Active control of flow separation over an airfoil using synthetic jets, *J. Fluid Struct.,* vol. **24**, no. 8, pp. 1349–1357, 2008.